

Enabling Massage Actions: An Interactive Parallel Robot with Compliant Joints

Huixu Dong, Yue Feng, Chen Qiu, Ye Pan, Miao He, I-Ming Chen, Fellow, *IEEE*

Abstract—We propose a parallel massage robot with compliant joints based on the series elastic actuator (SEA), offering a unified force-position control approach. First, the kinematic and static force models are established for obtaining the corresponding control variables. Then, a novel force-position control strategy is proposed to separately control the force-position along the normal direction of the surface and another two-direction displacement, without the requirement of a robotic dynamics model. To evaluate its performance, we implement a series of robotic massage experiments. The results demonstrate that the proposed massage manipulator can successfully achieve desired forces and motion patterns of massage tasks, arriving at a high-score user experience.

I. INTRODUCTION

Robotic manipulation technologies that are designed for domestic and workplace applications are engaging in physical activities [1-4], such as hands-on body massage [5]. Massage is in general a repetitive process, also a tedious, laborious, and time-consuming task. It is no surprise that an autonomous robot is an ideal worker that can replace a therapist to do the massage by initiating hands-on contact with humans.

Commercialized massage products, such as massage chairs and hammers, cannot usually reach users' satisfaction in their functional intelligence and prices [6, 7]. A two-end-effector massage device was developed to poke soft tissues [5], which cannot realize a compliant interaction. Jones *et al.* [8] presented a kneading robot for conducting the ring and linear massaging actions through an industrial robot, and Huang *et al.* developed a robot equipped with four elastic joints [9]; however, these robotic systems are expensive. An oral rehabilitation robot was applied to perform the rotational movement to rub the maxillofacial tissues of the face [10]. This device just has a single massage function. Kang *et al.* proposed a conceptual mechanism design for the robot implementing a tapping massage task, without the further implementation of a control strategy [11]. Some compliant mechanisms in interactive robots regulate the contact forces and conduct adaptable behaviors with

minimal control effort [12-14]. Compliant control has been thoroughly reviewed concerning the main two basic control such as hybrid force-position control and impedance control [15]. In addition, the emerging techniques promote the functional intelligence of massage robots. The point cloud was used for generating body trajectory for robot massage applications [16]. Si *et al.* allowed a massage robot to be more intelligent via the green Internet of Things [17]. For existing techniques, the high complexity, considerable cost and heavy structure of the mechatronics system result in the limitation of widespread applications [18].

To tackle the above problems, we develop a robotic manipulator which aims to assist physicians and conduct soft-tissue massage treatments for patients by the control of compliant movement to remain in contact with the interactive force (see Fig.1). The proposed massage robot can provide as follows: 1) it is convenient for this massage robot to be deployed at home or small clinics due to its compact and space-saving structure; 2) stable versatile massage treatments include pressing, tapping, rolling and pushing. The proposed parallel manipulator is made up of three symmetric fingers with proximal links, parallelogram links, and distal links connecting from the base to the end effector in parallel, which allows three translational motions and generally no rotational movement of the end effector [19]. Moreover, to guarantee safety, a rotary compliant joint with a series elastic actuator is designed and then, integrated into the manipulator; 3) safe and efficient massage treatment is implemented by a compliant control strategy. After constructing kinematic and static force models of the proposed massage robot, we design a control method that tracks force and position of a manipulator end-effector based on electronic encoders, which does not require the dynamics model and force sensor.

II. METHODOLOGY

A. Robot Kinematics Modelling

1) The geometry of the proposed massage robot

The kinematic chain of the proposed parallel manipulator is illustrated in Fig. 2. The fixed base and the end-effector Cartesian reference frame are denoted as $\{B\}$ and $\{P\}$, whose origins locate in their centers, respectively. In addition, the orientations of $\{B\}$ and $\{P\}$ are the same and thus, the rotation matrix ${}^B_R = I_3$ is constant. We have the active joint variables $\theta = \{\theta_1, \theta_2, \theta_3\}^T$ and the position variables

Huixu Dong is with Robot Perception and Grasp Lab, Zhejiang University, 310027 China; Yue Feng, I-Ming Chen are with Robotics Research Center, Nanyang Technological University, 639798 Singapore; Chen Qiu is with Maider Medical Industry Equipment Co., Ltd, 317607 China; Ye Pan is with Shanghai Jiaotong University, 200240 China; Miao He is with Chongqing University of Technology, 400054, China.



Figure 1. The design of the proposed parallel massage manipulator consisting of compliant joints, encoders, links and end-effector. A potential application scenario where the proposed massage robot can perform a tapping massage task (Middle figure).

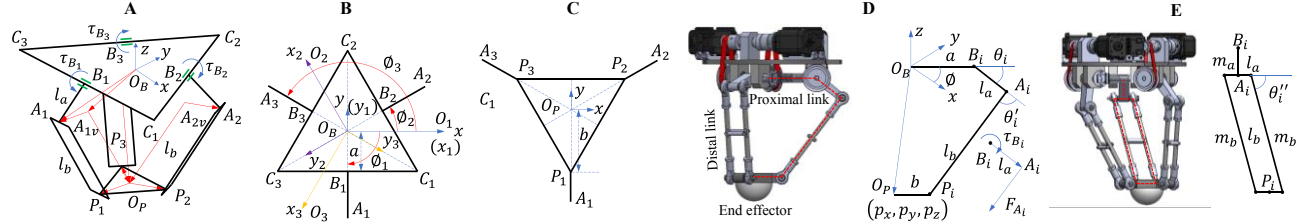


Figure 2. Geometry of the proposed parallel manipulator. The whole sketch(A); the fix-based platform with the coordinate reference frame O_B (B); the end-effector moving platform with the coordinate reference frame O_P (C); the two views of the manipulator (D and E). The green lines represent the actively rotational joints(A). x_i, y_i, z_i denote the coordinate reference frame and the corresponding axis x_i is parallel to the direction of the rotational joints (the green lines in A) at B_i ($i = 1, 2, 3$)(B). m_a and m_b represent the masses of the proximal rod (link) and distal rod (two rod consisting of link), respectively. l_a and l_b denote the proximal and distal link lengths, respectively.

$\{p_x, p_y, p_z\}^T$ of the end effector. To achieve the relationship between active joint and position variables, we build the following equation according to the vector-loop diagram with the kinematic parameters,

$$\overrightarrow{O_B B_i} + \overrightarrow{B_i A_i} + \overrightarrow{A_i P_i} = \overrightarrow{O_B O_P} + \overrightarrow{O_P P_i} \quad (1)$$

for $i = 1, 2, 3$, and thus, the geometrical constraints based on the distal link length can be described by

$$l_b = \|\overrightarrow{A_i P_i}\| = \|\overrightarrow{O_B O_P} + \overrightarrow{O_P P_i} - \overrightarrow{O_B B_i} - \overrightarrow{B_i A_i}\| \quad (2)$$

As shown in Fig. 2, B_i of the fixed-base revolute joint point in $\{B\}$ and P_i of the end-effector U-joint connection point in $\{P\}$ can be given as

$$\begin{aligned} {}^B B_1 &= \{0 \quad -a \quad 0\}^T, \\ {}^B B_2 &= \left\{ \frac{\sqrt{3}}{2}a \quad \frac{1}{2}a \quad 0 \right\}^T, \\ {}^B B_3 &= \left\{ -\frac{\sqrt{3}}{2}a \quad \frac{1}{2}a \quad 0 \right\}^T, \end{aligned} \quad (3)$$

$$\begin{aligned} {}^P P_1 &= \{0 \quad -b \quad 0\}^T, \\ {}^P P_2 &= \left\{ \frac{\sqrt{3}}{2}b \quad \frac{1}{2}b \quad 0 \right\}^T, \\ {}^P P_3 &= \left\{ -\frac{\sqrt{3}}{2}b \quad \frac{1}{2}b \quad 0 \right\}^T, \end{aligned} \quad (4)$$

According to the active joint variables $\{\theta_1, \theta_2, \theta_3\}^T$, we can obtain the vector $\overrightarrow{B_i A_i}$ of the fixed-base revolute joint point in $\{B\}$

$$\begin{aligned} \overrightarrow{B_1 A_1} &= \{0 \quad -l_a \cos \theta_1 \quad -l_a \sin \theta_1\}^T, \\ \overrightarrow{B_2 A_2} &= \{l_a \cos \theta_2 \cos \phi_2 \quad l_a \cos \theta_2 \sin \phi_2 \quad -l_a \sin \theta_2\}^T, \\ \overrightarrow{B_3 A_3} &= \{-l_a \cos \theta_3 \cos \phi_3 \quad l_a \cos \theta_3 \sin \phi_3 \quad -l_a \sin \theta_3\}^T, \end{aligned} \quad (5)$$

where $\phi_i = -\frac{\pi}{2} + \frac{2\pi}{3}(i-1)$, $i = 1, 2, 3$; a and b represent the radii of the fixed and end-effector platform, respectively; l_a and l_b are the proximal/upper and

distal/lower link lengths, respectively; ϕ_i denotes the rotation angle concerning the z axis for the point B_i in $\{B\}$; the actuated joint angle is represented by θ_i and passive joint angles are indicated by θ'_i and θ''_i (see Fig. 2). Thus, we have $\overrightarrow{A_i P_i}$ as follows

$$\begin{aligned} \overrightarrow{A_1 P_1} &= \{p_x \quad p_y + l_a \cos \theta_1 + k \quad p_z + l_a \sin \theta_1\}^T, \\ \overrightarrow{A_2 P_2} &= \begin{cases} p_x - l_a \cos \theta_2 \cos \phi_2 + m \\ p_y - l_a \cos \theta_2 \sin \phi_2 + n \\ p_z + l_a \sin \theta_2 \end{cases} \\ \overrightarrow{A_3 P_3} &= \begin{cases} p_x + l_a \cos \theta_3 \cos \phi_3 - m \\ p_y - l_a \cos \theta_3 \sin \phi_3 + n \\ p_z + l_a \sin \theta_3 \end{cases} \end{aligned} \quad (6)$$

in which $k = a - b$, $m = \frac{\sqrt{3}}{2}b - \frac{\sqrt{3}}{2}a$, $n = \frac{1}{2}b - \frac{1}{2}a$.

The following kinematics equations for the proposed manipulator are obtained as

$$\|\overrightarrow{A_i P_i}\|^2 - l_b^2 = 0 \quad (7)$$

which can be further utilized to conduct forward and inverse position kinematics analysis.

2) Inverse position kinematics (IPK)

In terms of inverse position kinematics, the Cartesian position $\{p_x, p_y, p_z\}^T$ of the end-effector is provided to calculate the three actuated revolute joint angles $\{\theta_1, \theta_2, \theta_3\}^T$. Referring to Eq.(7), it can be further described as

$$E_i \cos \theta_i + F_i \sin \theta_i + G_i = 0 \quad (8)$$

which can be addressed through the tangent half-angle substitution. If we define

$$t_i = \tan \frac{\theta_i}{2}, \quad \cos \theta_i = \frac{1-t_i^2}{1+t_i^2}, \quad \sin \theta_i = \frac{2t_i}{1+t_i^2}, \quad (9)$$

then Eq.(8) can be rearranged as

$$(G_i - E_i)t_i^2 + (2F_i)t_i + (G_i + E_i) = 0 \quad (10)$$

If $E_i^2 + F_i^2 > G_i^2$, we can obtain

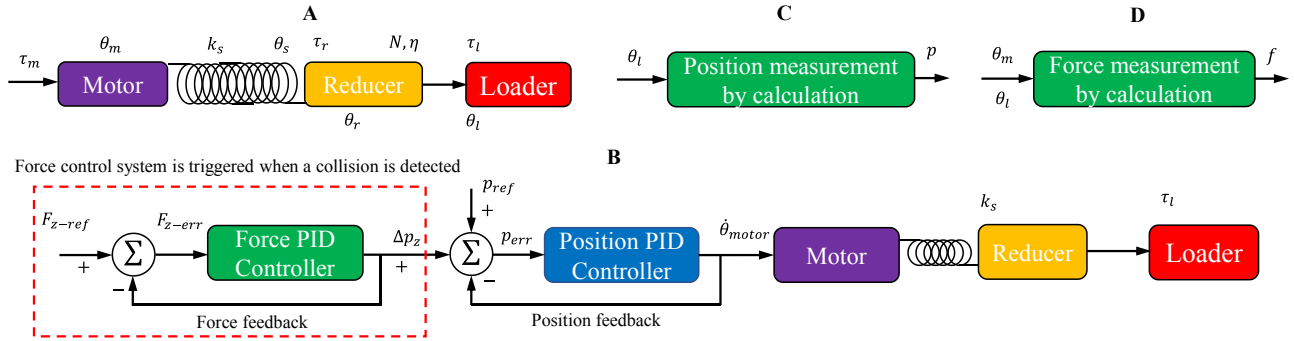


Figure 3. The diagram of the transmission model of the compliant joint(A), the overview of the compliant actuator system(B), the force(C) and position(D) measurements by calculations. F_{z-ref} and p_{ref} denote the z-axis pre-defined force and the pre-defined position (p_x, p_y, p_z), respectively; Δp_z represents the z-axis changed position determined by the force control system; F_{z-err} and p_{err} indicate the z-axis force error and the position error, respectively; $\dot{\theta}_{motor}$ is the velocity of the motor.

$$t_{i,1,2} = \frac{-F_i \pm \sqrt{E_i^2 + F_i^2 - G_i^2}}{G_i - E_i} \quad (11)$$

and

$$\theta_i = 2 \tan^{-1}(t_i) \quad (12)$$

Note that two θ_i are both valid solutions.

3) Forward position kinematics(FPK)

Given the three actuated joint angles $\{\theta_1, \theta_2, \theta_3\}^T$, the resulting Cartesian position of the end-effector moving platform is obtained. According to the vector loop, we have

$$\overline{O_B B_i} + \overline{B_i A_i} = \overline{O_B A_i} \quad (13)$$

which are

$$\begin{aligned} {}^B \overline{O_B A_1} &= \{0 \quad -a - l_a \cos \theta_1 \quad -l_a \sin \theta_1\}^T \\ {}^B \overline{O_B A_2} &= \left\{ \begin{array}{l} \frac{\sqrt{3}}{2}(a + l_a \cos \theta_2) \\ \frac{1}{2}(a + l_a \cos \theta_2) \\ -l_a \sin \theta_2 \end{array} \right\} \\ {}^B \overline{O_B A_3} &= \left\{ \begin{array}{l} -\frac{\sqrt{3}}{2}(a + l_a \cos \theta_3) \\ \frac{1}{2}(a + l_a \cos \theta_3) \\ -l_a \sin \theta_3 \end{array} \right\} \end{aligned} \quad (14)$$

If we define three virtual sphere centers based on ${}^B P = I_3$ through

$$\overline{O_B A_i} - \overline{O_P P_i} = \overline{O_B A_{iv}} \quad (15)$$

$$\begin{aligned} {}^B \overline{O_B A_{1v}} &= \{\overline{O A_{1x}} \quad \overline{O A_{1y}} \quad \overline{O A_{1z}}\}^T \\ {}^B \overline{O_B A_{2v}} &= \{\overline{O A_{2x}} \quad \overline{O A_{2y}} \quad \overline{O A_{2z}}\}^T \\ {}^B \overline{O_B A_{3v}} &= \{\overline{O A_{3x}} \quad \overline{O A_{3y}} \quad \overline{O A_{3z}}\}^T \end{aligned}$$

$$\begin{aligned} \overline{O A_{1x}} &= 0, \\ \overline{O A_{1y}} &= -a - l_a \cos \theta_1 + b, \\ \overline{O A_{1z}} &= -l_a \sin \theta_1, \\ \overline{O A_{2x}} &= \frac{\sqrt{3}}{2}(a + l_a \cos \theta_2) - \frac{\sqrt{3}}{2}b, \\ \overline{O A_{2y}} &= \frac{1}{2}(a + l_a \cos \theta_2) - \frac{1}{2}b, \\ \overline{O A_{2z}} &= -l_a \sin \theta_2, \\ \overline{O A_{3x}} &= -\frac{\sqrt{3}}{2}(a + l_a \cos \theta_3) + \frac{\sqrt{3}}{2}b, \end{aligned}$$

$$\begin{aligned} \overline{O A_{3y}} &= \frac{1}{2}(a + l_a \cos \theta_3) - \frac{1}{2}b, \\ \overline{O A_{3z}} &= -l_a \sin \theta_3, \end{aligned}$$

then the FPK solution is the intersection point of three known spheres. Let a sphere be referred as a vector $(\{c\}, r)$ with the center $\{c\}$ and scalar radius r . Thus, the FPK unknown point is the intersection of the three known spheres $(\{{}^B A_{iv}\}, l_b)$. Assume the three given spheres are (c_i, l_b) where $c_i = \{x_i, y_i, z_i\}^T$ and radii l_b are known. The equations of the three spheres are provided as

$$(x - x_i)^2 + (y - y_i)^2 + (z - z_i)^2 = l_b^2 \quad (16)$$

Then, we expand the equations above and subtract the third from the first and the third from the second, yielding

$$\begin{aligned} x &= f(y) \\ z &= f(y) \end{aligned} \quad (17)$$

These two functions are substituted into the sphere equation for obtaining the position of the moving end-effector.

B. Static Force Analysis

1) The transmission model of compliant joint

Figure 3(A) illustrates the transmission of the compliant joint based on the series elastic actuator (SEA). This system consists of a motor, a synchronous belt that amplifies the output force (torque) of the actuator, a spring placed between the motor and a synchronous belt, and the loader (parallel manipulator). To simplify the dynamic model, we consider the compliant joint based on SEA as an undamped linear torsion spring. As shown in Fig. 3(A), through the spring, the torques can be formulated as

$$\tau_m = \tau_r = k_s \theta_s = \frac{\tau_l}{N\eta} \quad (18)$$

where τ_m is the output torque of the motor (the input torque of the compliant element-torsion spring); τ_r denotes the output torque of the torsion spring; k_s is the spring stiffness; $N = 2$ is the reduction ratio of the synchronous belt and η is the transmission efficiency, respectively; θ_s represents the changed angle from the input angle θ_m to the output angle θ_r of the compliant element, which is given as

$$\theta_s = \theta_m - \theta_r = \theta_m - N\theta_l \quad (19)$$

in which θ_l represents the angle of the load. Combining Eq.(18) and Eq.(19), we have

$$\tau_l = k_s N \eta (\theta_m - N\theta_l) \quad (20)$$

2) The resultant force of the end-effector

After achieving the end-effector position $\{p_x, p_y, p_z\}^T$ by the above algorithm, we do the static analysis to calculate the resultant force of the end-effector.

To obtain the unit vector of $\overrightarrow{A_i P_i}$ ($i = 1, 2, 3$) in Eq.(6), we calculate the magnitude $\|\overrightarrow{A_i P_i}\|$ of $\overrightarrow{A_i P_i}$ with the coordinate reference frame O_B as follows,

$$\|\overrightarrow{A_i P_i}\| = \sqrt{X^2 + Y^2 + Z^2} \quad (21)$$

where X, Y, Z represent the three components of a vector.

Thus, the unit vector $\|\overrightarrow{e A_i P_i}\|$ is given as

$$\overrightarrow{e A_i P_i} = \frac{\overrightarrow{A_i P_i}}{\|\overrightarrow{A_i P_i}\|} \quad (22)$$

To allow the coordinate of the unit vector of $\overrightarrow{A_i P_i}$ to be consistent with that of the loading torque at each proximal link, we need to respectively convert three unit vectors $\{\overrightarrow{e A_1 P_1}, \overrightarrow{e A_2 P_2}, \overrightarrow{e A_3 P_3}\}$ in the coordinate reference frame O_B to the coordinate reference frames $\{O_1 - (x_1, y_1, z_1), O_2 - (x_2, y_2, z_2), O_3 - (x_3, y_3, z_3)\}$, as shown in Fig. 2(B). Note that the x -axes of these three coordinate frames are parallel to the rational axes of three proximal links on the base. In particular, the coordinate reference frame O_1 coincides with the base coordinate reference frame O_B ; O_2 is the frame that O_B is counterclockwise rotated $\frac{2}{3}\pi$ to form; O_3 is clockwise rotated $\frac{2}{3}\pi$ to obtain O_3 . Further, we use the two rotation matrices R_{B-2}^z and R_{B-3}^z to convert the unit vectors $\overrightarrow{e A_2 P_2}$ and $\overrightarrow{e A_3 P_3}$ to the coordinate reference frames O_2 and O_3 , respectively. The rotation matrices R_{B-2}^z and R_{B-3}^z are provided as

$$R_{B-2}^z = \begin{bmatrix} \cos\left(\frac{2}{3}\pi\right) & -\sin\left(\frac{2}{3}\pi\right) & 0 \\ \sin\left(\frac{2}{3}\pi\right) & \cos\left(\frac{2}{3}\pi\right) & 0 \\ 0 & 0 & 1 \end{bmatrix}$$

$$R_{B-3}^z = \begin{bmatrix} \cos\left(-\frac{2}{3}\pi\right) & -\sin\left(-\frac{2}{3}\pi\right) & 0 \\ \sin\left(-\frac{2}{3}\pi\right) & \cos\left(-\frac{2}{3}\pi\right) & 0 \\ 0 & 0 & 1 \end{bmatrix} \quad (23)$$

Therefore, the unit vectors $\overrightarrow{e A_1 P_1}$, $\overrightarrow{e A_2 P_2}$ and $\overrightarrow{e A_3 P_3}$ can be calculated by

$$\begin{aligned} \overrightarrow{e A_1 P_1} &= \overrightarrow{e A_1 P_1} \\ \overrightarrow{e A_2 P_2} &= R_{B-2}^z \cdot \overrightarrow{e A_2 P_2} \\ \overrightarrow{e A_3 P_3} &= R_{B-3}^z \cdot \overrightarrow{e A_3 P_3} \end{aligned} \quad (24)$$

In the 3D space, the torque is given by the cross product of the position vector(distance vector) and the force vector, such as $\tau = \vec{r} \times \vec{F}$ (τ representing the torque, \vec{r} indicating the distance vector as well as \vec{F} denoting the force vector). Employing this method, we can calculate the force magnitudes $F_{A_1}, F_{A_2}, F_{A_3}$ acting on points A_1, A_2, A_3 in the coordinate reference frames $\{O_1, O_2, O_3\}$, respectively. In particular, we have the following equations as

$$\begin{aligned} l_a \times F_{A_1} \cdot \overrightarrow{e A_1 P_1} &= \tau_{B_1} \\ l_a \times F_{A_2} \cdot \overrightarrow{e A_2 P_2} &= \tau_{B_2} \\ l_a \times F_{A_3} \cdot \overrightarrow{e A_3 P_3} &= \tau_{B_3} \end{aligned} \quad (25)$$

where τ_{B_i} ($i = 1, 2, 3$) represents the loading torque at the rotation joint B_i . The value of τ_{B_i} along the x -axis of the coordinate reference frame O_i is known, which is equal to τ_i for each motor. There is just one unknown force magnitude for one item of Eq.(22) and thus, we can obtain these force magnitudes. After that, F_{A_2} in O_2 and F_{A_3} in O_3 need to be converted to the coordinate reference frame $O_B(O_1)$ by the matrices R_{B-3}^z and R_{B-2}^z as follows,

$$\begin{aligned} {}^B F_{A_1} &= F_{A_1} \\ {}^B F_{A_2} &= R_{B-3}^z F_{A_2} \\ {}^B F_{A_3} &= R_{B-2}^z F_{A_3} \end{aligned} \quad (26)$$

in which ${}^B F_{A_i}$ ($i = 1, 2, 3$) indicates the force vector along $A_i P_i$ in the coordinate reference frame O_B . Finally, the resultant force ${}^B F_{ee}$ of the end-effector can be provided as

$${}^B F_{ee} = {}^B F_{A_1} + {}^B F_{A_2} + {}^B F_{A_3} \quad (27)$$

C. Control System Design of the Robotic Manipulator

In practical applications, the massage manipulator has a relatively small workspace and small motion speed. Moreover, the proximal and distal links are relatively light. Thus, we implement the control strategy of the parallel massage manipulator without a dynamic model of the robot.

To achieve such a target of the manipulator performing massage tasks, we design a control system including the rear-loop position and the front-loop force, as shown in Fig. 3(B). For each loop, we adopt the PID feedback control strategy. As illustrated in Fig. 3(C, D), the built-in encoder of a motor and the encoder mounted on the rotation shaft of the proximal link can provide θ_m and θ_l , respectively. To perform the path planning of the end-effector, its position can be obtained by the forward kinematics (see Fig. 3-C) at the corresponding time sample when the angle θ_l of the load is known and then, the static force analysis can be applied to determine the force of the end-effector. Further, we put θ_m and θ_l into Eq.(20) to obtain τ_i for calculating the end-effector's force. In terms of massage tasks, the robotic manipulator generally needs to guarantee that the force exerted on the skin tissue of the human body is constant along the z -axis direction.

III. EXPERIMENTS

A) Evaluations of the Massage System

In Eq.(20), k_s and η need to be confirmed for calculating the force of the end-effector. An electronic scale with a resolution of 0.005kg below the massage robot is considered as a force sensor to collect the contacting forces from the manipulator's end-effector. We allow the massage manipulator to touch the surface of the electronic scale, gradually increasing the z -axis position. Comparing the force calculated via the proposed static force model with the force measured by the electronic scale, we can obtain the errors of the calculated force in practical applications for adjusting the spring stiffness and the transmission efficiency, thus determining $k_s = 1, \eta = 1$.

1) Evaluation of hybrid force&position control

For evaluating the performance of the proposed massage

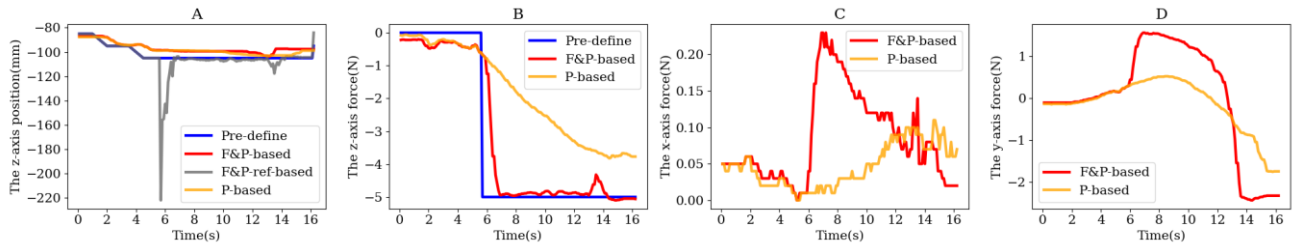


Figure 4. The z-axis position (A), the z-axis forces (B), the x-axis forces(C) and the y-axis forces(D) at the time samples. The blue, yellow, orange curves represent the pre-defined trajectory or force as a reference value (Pre-define), the trajectory or force based on the pure position control(P-based), respectively. The grey curve indicates the z-axis pre-defined reference trajectory for hybrid force&position control(F&P-based-ref)(A). For the grey curve, initially, its z-axis trajectory overlaps the pre-define trajectory represented by the blue curve. During this period, the force control is not triggered since the pressing force is smaller than the set triggered threshold of 0.6N. Next, with the z-axis force increasing, the force control is triggered at around 5.6s. The z-axis position generates a sudden change since the z-axis changing position Δp_z is involved in this pre-defined trajectory(see Fig.4-B). Further, this pre-defined trajectory for force-position control still goes back and almost overlaps the pre-defined trajectory.

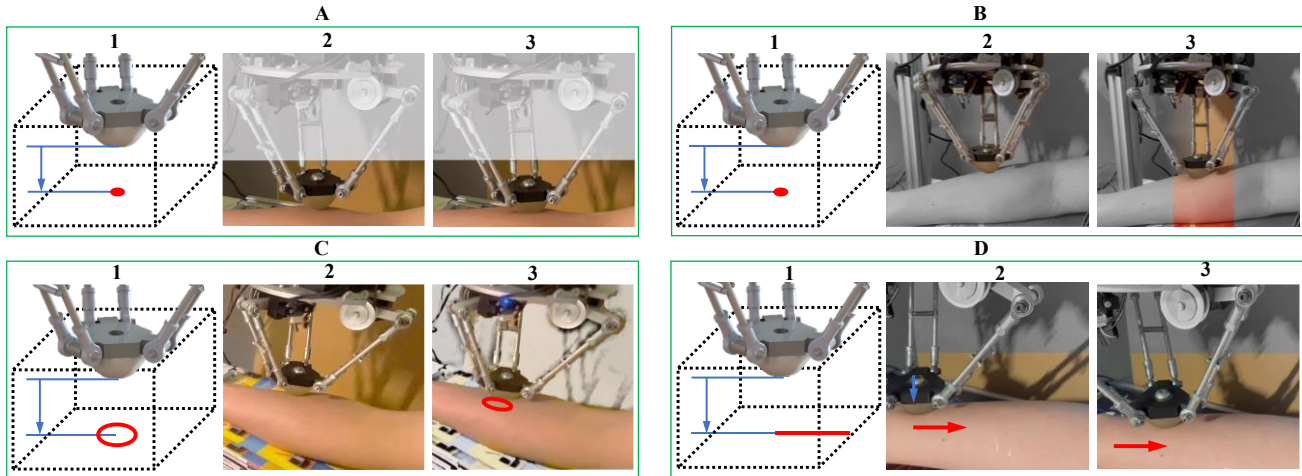


Figure 5. The pressing(A), tapping(B), rolling(C) and pushing(D) massage tasks. The positions of the pressing and tapping massage tasks(A-1, B-1); the trajectories of the rolling and pushing massage tasks(C-1, D-1); the snapshots of the massage tasks(A-1-2, B-1-2, C-1-2, D-1-2). The black cubic denotes the workspace and the blue arrow indicates the moving direction of the end-effector. The red tiny circle and the red line represent the trajectories of the rolling and pushing massage tasks, respectively(C, D).

manipulator on the proposed force-position control, we conducted two groups of comparison experiments on the same experimental platform, including the pure position control and hybrid force&position control (force-position control). For the setup of position control, the manipulator was allowed to move along the y-axis from $p_y = 20$ to $p_y = -20mm$ with $p_x = 0$ and $p_z = -105mm$ at a constant speed. Since the surface of the electronic scale is at $p_z = -101mm$, the manipulator generates a pressing force F_z in the z-axis direction and frictional forces in the x-axis and y-axis directions. The end-effector has surface contact with the electronic scale, which results in the x-axis and y-axis frictions. In terms of force-position control, based on the above setup, we enable the force control loop to be triggered when F_z is bigger than 0.6 N and set a reference force $F_{z-ref} = 5N$ in the force control loop (see Fig. 4).

Figure 4(A) illustrates two scenarios where the end-effector follows the pre-defined trajectory and force under the pure position control and force-position control strategies. First, in terms of position control, the pre-defined (blue curve) and position-control (yellow curve) trajectories have similar changing trends and the average tracking difference of this

trajectory keeps small values. This indicates that the used position control can enable the end-effector to accurately follow the pre-defined trajectory. The position tracking difference is generated owing to the mechanical backlash. Second, we evaluate the proposed force-position strategy. For the electronic scale, the measured force is in proportion to the z-axis displacement. That is, if the z-axis position is a constant, the applied force on the surface of the electronic scale remains unchanged. It is found that the z-axis trajectory based on the force-position control strategy is almost the same as the z-axis control-based trajectory. Thus, the proposed force-position control strategy can enable the end-effector to track the pre-defined trajectory and force.

The z-axis position control-based force F_{z-p} and the force-position control-based F_{z-fp} are calculated by the proposed method of the static force analysis, as illustrated in Fig. 4(B). The pre-defined force is considered as a reference force in the force control loop. While tracking, F_{z-p} also increases as the end-effector needs to arrive at the pre-defined z-axis position; however, the force tracking based on the position control has unsatisfied performance such as a severe delay and big force error. Contrastively, the tracking performance of F_{z-fp} is

superior to that of F_{z-p} owing to the involved force control. Although a small force fluctuation occurs at 13.7s, F_{z-fp} can still successfully continue tracking the reference force.

The results of forces in the x-axis and y-axis directions are obtained by the proposed static force model and encoders, as illustrated in Fig. 4(C, D). The forces in the x-axis direction have small fluctuations compared to those in the y-axis direction. For the x-axis forces, this is somewhat expected since there are just frictional forces, without the x-axis force control (see Fig. 4-C). Moreover, since F_{z-p} is smaller than F_{z-fp} , the frictional force based on the position control is less than one based on the force-position control (see Fig. 4-C, D).

B) Robot Massage Tasks

A series of experiments were carried out for investigating the massage effectiveness of the proposed manipulator (see Fig. 5), which is provided as follows:

- **Pressing:** the end-effector moves to a destination which is generally an acupuncture point, goes down gently, gradually increases the force until the pre-defined force is reached, and remains stationary for a while with this force.
- **Taping:** the robotic end-effector moves to a pre-taping position above the destination, which is generally an acupuncture point, goes down rapidly with an adjustable force until the pre-defined force is reached.
- **Rolling:** the robot end-effector moves to a destination which is generally an acupuncture point, goes down gently, gradually increases the force until the pre-defined force arrives, and then, moves periodically in the pattern of the tiny circle on the point with a fixed downward force.
- **Pushing:** the robotic end-effector moves to a destination which is generally an acupuncture point, goes down slowly with an adjustable force, then it pushes straight along the pre-defined trajectory with a fixed downward force.

We gathered feedback from their experiences. Overall, users' experience with the proposed robot surpassed their expectations, as reflected in their comments: "I got very comfortable with it". The proposed massage manipulator can successfully implement multiple massage tasks on humans, which is potentially employed in small clinics and household scenarios.

IV. CONCLUSION

In this work, we established a novel parallel massage manipulator that can implement multiple-functional massage tasks and be potentially deployed in small clinics and households due to the suitable structure and low cost. Various experiments were performed to demonstrate that the proposed massage robot could successfully provide treatment aids for physicians.

ACKNOWLEDGEMENT

This work is partially supported by Science Fund for Creative Research Groups of National Natural Science Foundation of China (No.51821093).

REFERENCES

- [1] H. Dong, E. Asadi, G. Sun, D. K. Prasad, and I.-M. Chen, "Real-time robotic manipulation of cylindrical objects in dynamic scenarios through elliptic shape primitives," *IEEE Transactions on Robotics*, vol. 35, no. 1, pp. 95-113, 2018.
- [2] H. Dong, C.-Y. Chen, C. Qiu, C.-H. Yeow, and H. Yu, "GSG: A Granary-shaped Soft Gripper with Mechanical Sensing via Snap-Through Structure," *IEEE Robotics and Automation Letters*, 2022.
- [3] H. Dong, D. K. Prasad, and I.-M. Chen, "Object pose estimation via pruned hough forest with combined split schemes for robotic grasp," *IEEE Transactions on Automation Science and Engineering*, vol. 18, no. 4, pp. 1814-1821, 2020.
- [4] H. Dong, D. K. Prasad, Q. Yuan, J. Zhou, E. Asadi, and I.-M. Chen, "Efficient pose estimation from single RGB-D image via Hough forest with auto-context," in *2018 IEEE/RSJ International Conference on Intelligent Robots and Systems (IROS)*, 2018: IEEE, pp. 7201-7206.
- [5] M. Kume, Y. Morita, Y. Yamauchi, H. Aoki, M. Yamada, and K. Tsukamoto, "Development of a mechanotherapy unit for examining the possibility of an intelligent massage robot," in *Proceedings of IEEE/RSJ International Conference on Intelligent Robots and Systems. IROS'96*, 1996, vol. 1: IEEE, pp. 346-353.
- [6] S. W. Cheatham and M. J. Kolber, "Does roller massage with a foam roll change pressure pain threshold of the ipsilateral lower extremity antagonist and contralateral muscle groups? An exploratory study," *Journal of sport rehabilitation*, vol. 27, no. 2, pp. 165-169, 2018.
- [7] W. Wang, P. Zhang, C. Liang, and Y. Shi, "Design, path planning improvement and test of a portable massage robot on human back," *International Journal of Advanced Robotic Systems*, vol. 15, no. 4, p. 1729881418786631, 2018.
- [8] K. C. Jones and W. Du, "Development of a massage robot for medical therapy," in *Proceedings 2003 IEEE/ASME International Conference on Advanced Intelligent Mechatronics (AIM 2003)*, 2003, vol. 2: IEEE, pp. 1096-1101.
- [9] Y. Huang, J. Li, Q. Huang, and C. Liu, "Design and control of anthropomorphic BIT soft arms for TCM remedial massage," in *2013 IEEE/RSJ International Conference on Intelligent Robots and Systems*, 2013: IEEE, pp. 1960-1965.
- [10] H. Koga et al., "Development of oral rehabilitation robot for massage therapy," in *2007 6th International Special Topic Conference on Information Technology Applications in Biomedicine*, 2007: IEEE, pp. 111-114.
- [11] C.-g. Kang, B.-j. Lee, I.-x. Son, and H.-y. Kim, "Design of a percussive massage robot tapping human backs," in *RO-MAN 2007-The 16th IEEE International Symposium on Robot and Human Interactive Communication*, 2007: IEEE, pp. 962-967.
- [12] Z. Wang et al., "Design of a novel compliant safe robot joint with multiple working states," *IEEE/ASME Transactions on Mechatronics*, vol. 21, no. 2, pp. 1193-1198, 2015.
- [13] H. Dong, E. Asadi, C. Qiu, J. Dai, and I.-M. Chen, "Geometric design optimization of an under-actuated tendon-driven robotic gripper," *Robotics and Computer-Integrated Manufacturing*, vol. 50, pp. 80-89, 2018.
- [14] H. Dong, E. Asadi, C. Qiu, J. Dai, and I.-M. Chen, "Grasp analysis and optimal design of robotic fingertip for two tendon-driven fingers," *Mechanism and Machine Theory*, vol. 130, pp. 447-462, 2018.
- [15] M. Schumacher, J. Wojtusich, P. Beckerle, and O. von Stryk, "An introductory review of active compliant control," *Robotics and Autonomous Systems*, vol. 119, pp. 185-200, 2019.
- [16] R. C. Luo, S. Y. Chen, and K. C. Yeh, "Human body trajectory generation using point cloud data for robotics massage applications," in *2014 IEEE International Conference on Robotics and Automation (ICRA)*, 2014: IEEE, pp. 5612-5617.
- [17] W. Si, G. Srivastava, Y. Zhang, and L. Jiang, "Green internet of things application of a medical massage robot with system interruption," *IEEE Access*, vol. 7, pp. 127066-127077, 2019.
- [18] Y.-C. Wang, C.-Y. Wu, and P.-C. Chung, "Constraint-based correspondence matching for stereo-based interactive robotic massage machine," *Journal of Intelligent & Robotic Systems*, vol. 72, no. 2, pp. 179-196, 2013.
- [19] J.-P. Merlet, *Parallel robots*. Springer Science & Business Media, 2005.